Electron Beam Crystallization of Amorphous Silicon Thin Films

Stefan Saager
Fraunhofer Institute for Organic Electronics, Electron Beam and Plasma Technology (FEP)
Winterbergstrasse 28, 01277 Dresden, Germany, Stefan.Saager@fep.fraunhofer.de

Abstract: In microelectronics and photovoltaics, there is a huge need for fabrication of crystalline silicon (Si) thin films with excellent material properties and with minimum production cost at the same time. This paper deals with the first realization steps of mentioned efforts by a novel production method. For this the crystallization of amorphous silicon (a-Si) thin films by an electron beam (EB) treatment was tested. EB processing by line scanning led to the formation of a narrow grained polycrystalline structure and leads to an undesired layer delamination with increasing EB power density. By adapting process parameters an epitaxial layer regrowth with similar crystallographic orientation as the (001) Si substrate could be reached.
With the help of COMSOL® simulations of the temperature and stress field during EB crystallization process observed experimental results could be fathomed, e.g. reason for layer delamination, and process improvements could be derived.

Keywords: electron beam crystallization, silicon thin films, thin film photovoltaics, explosive solid phase crystallization, rapid thermal processing,

1. Introduction

A promising method for low cost production of efficient silicon thin film solar cells is the electron beam physical vapor deposition (EB-PVD) of high purity Si absorber layers with high deposition rates up to $300\,\mathrm{nm/s}$ [1, 2] followed by a crystallization step [3]. For liquid phase crystallization the deposited Si layer usually is encapsulated by a SiN_x/SiO_x layer stack for avoiding agglomeration, followed by heating-up in a narrow zone to silicon's melting temperature (1685 K) by laser [4], by EB [5] or by lamps [6]. With this procedure, solar cell efficiencies up to 11.5 % could be reached up to now [7]. But crystallization from liquid phase offers some drawbacks:

- There is a potential risk for taking up contaminations of Si melt from substrate and encapsulation
- Encapsulation has to be removed afterwards
- Formation of elongated grains in lateral pull direction results in recombination defects at grain boundaries
- The maximum crystallization speed in lateral direction is limed to some $\mathrm{cm/s}$ [3]
- Due to the high temperature and small process speed the substrate has to withstand large thermal loads [8]

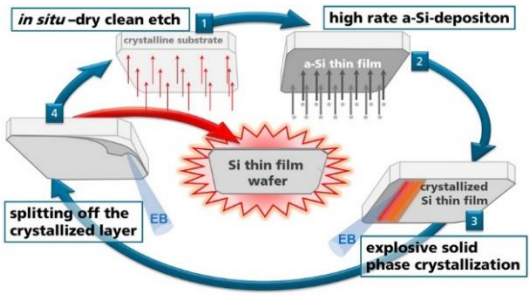

Figure 1: Concept for kerfless wafering using electron beam (EB) technology in a cycle process. The crystalline substrate, e.g. silicon or sapphire wafer, will be reused after splitting of crystallized Si thin film.

An alternative approach to encapsulation could be kerfless wafering [9] (Figure 1): First cleaning single crystalline substrate (c-Si) *in situ* [10], second depositing an a-Si layer on it and third crystallizing the a-Si layer in the solid phase regime by EB. Due to the ability to adjust electron penetration range R_e and corresponding the power-depth relation f_A by tuning the EB energy ($E_{e^-} = eU_B$) [2] an epitaxial regrowth could be reached, starting from the cleaned single crystalline substrate interface (Figure 2). In a fourth step the crystallized layer can be split off by a subsequent EB process step with re-adjusted EB parameters [11].

To specify the relevant parameter region by experiments affords an extensive diligence and interim results are often hard to interpret. Therefore the simulation of undetectable process states, e. g. the temperature and stress field, represents a comfortable way for process development and optimization.

This paper presents first EB crystallization experiments in the solid phase regime and justifies observed results by finite element method (FEM) simulations.

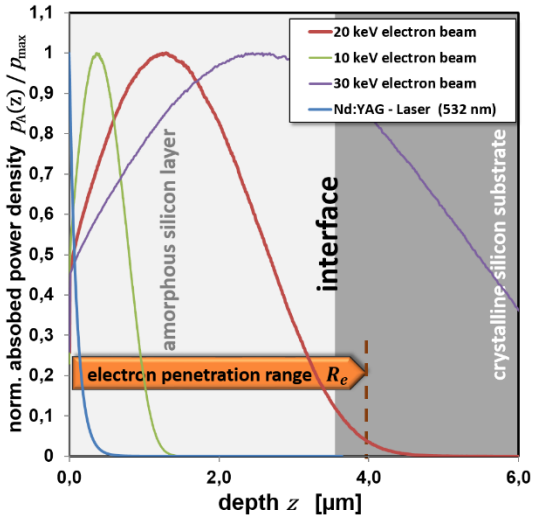

Figure 2: The depth relation of the absorbed power density in a thin-film system can be easily tuned for EB (red) by acceleration voltage in contrast to laser (blue).

2. Governing Equations

For the power source, represented by a focused electron beam (EB), a current density profile $j_B(x,y)$ (Eq. 1) with a GAUSSIAN shape was assumed reaching an electron beam diameter of $d_F \approx 600$ µm. Incidentally, the validity of the profile was also checked experimentally by FARADAY-cup measurements.

$$j_B(x,y,t) = \frac{I_B}{\pi r_F^2} e^{\frac{x^2+(y-v_y t)^2}{r_F^2}} \quad \text{Eq. 1}$$

(See Table 1 in Appendix for symbol description!)

With these assumption, the transient temperature field and thermal induced stress during EB treatment were calculated by FEM simulations using *COMSOL*® software. Temperature field was calculated by numerically solving the three-dimensional heat equation with temperature dependent material properties (Eq. 2).

$$c_p(T)\rho(T)\frac{\partial T(\vec{r},t)}{\partial t} - \nabla[\lambda(T)\cdot\nabla T(\vec{r},t)] = p_A(\vec{r},t) - \rho(T)\frac{\partial h_{\text{fus}}}{\partial t} \quad \text{Eq. 2}$$

For the inhomogeneous term in the heat equation, a spatial distributed heat generation density $p_A(\vec{r},t)$ was assumed, according to the absorbed EB power density (Eq. 3), as well as melting and solidification effects were considered by specific enthalpy of fusion h_{fus}.

$$p_A(x,y,z,t) = \eta_{th} U_B \cdot j_B(x,y,t)\frac{f_A(z)}{R_e} \quad \text{Eq. 3}$$

Ambient heat exchange by thermal radiation was taken into account only, because EB process is carried out under vacuum conditions at initial room temperature, where thermal contact is low.

Due to thermal expansion, the stress tensor $\hat{\sigma}$ is deducted from Eq. 4 by computing the thermal strain tensor with Eq. 6 from temperature field.

$$\hat{\sigma} = \hat{\sigma}_{ini} + \hat{C}:\hat{\epsilon}^{\sigma} \quad \text{Eq. 4}$$
$$\hat{\epsilon}^{\sigma} = \hat{\epsilon} - \hat{\epsilon}_0 - \hat{\epsilon}^{\text{th}} \quad \text{Eq. 5}$$
$$\hat{\epsilon}^{\text{th}} = \hat{\alpha}(T)\cdot(T(\vec{r}) - T_{\text{ref}}) \quad \text{Eq. 6}$$

Initial layer tensile stress of $\sigma_{ini} \approx +200$ MPa, a common value for the deposited films [12], was also taken into account.

Nevertheless, in order to evaluate the effects of stress accumulation on layer delamination, one needs to consider the elastic strain energy density w_σ (Eq. 7).

$$w_\sigma = \frac{1}{2}\cdot\int_0^d \hat{\sigma}:\hat{\epsilon}^{\sigma}\,\mathrm{d}z \quad \text{Eq. 7}$$

3. Methods

Previous crystallization experiments test samples were fabricated. They consist of single crystalline 10×10 mm² (001) Si substrates, which were coated with $d = 1$ µm and $d = 3.6$ µm thick pure a-Si thin film, respectively. To ensure excellent material properties a high layer purity is needed. Therefore Si substrates were cleaned by RCA-method *ex situ* and by EB dry clean etch *in situ* [10], previously, and the a-Si deposition was carried out by crucible-free EB-PVD, described in detail earlier [13]. The amorphousness of the thin film were ensured by limiting the substrate temperature to ≈ 200 °C during deposition.
Crystallization was accomplished by EB processing after coating and cooling down the substrates to room temperature. The focused EB was scanned over the coated substrate at an electron energy of $E_e = 20$ keV. This corresponds to an electron penetration range of $R_e \approx 4$ µm, which is in same order of layer thickness. High energy density input was realized by scanning the EB along a line with various scanning speed and constant EB power. Lower energy density input was implemented by using an extended scanning pattern with high repletion rate at lower EB power.

4. Numerical Model

Simulations were carried out principally to clarify crystallization and delamination phenomena. In a coupled study using *COMSOL® Multiphysics* Heat Transfer and Structural Mechanics Modules the transient temperature field and thermal induced stress were calculated. Therefore, a 3D model with a swept mesh was generated, representing the layer-substrate-system (Figure 3).

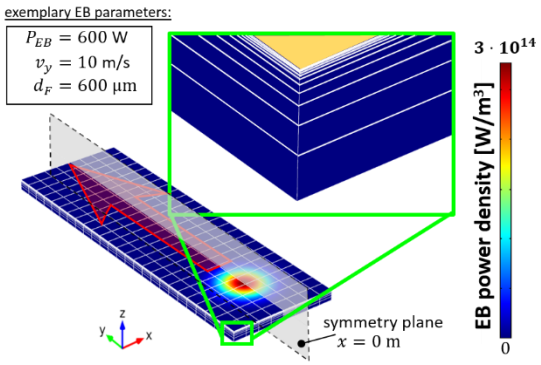

Figure 3: Used geometry with swept mesh and moving heat source due to EB treatment. For the c-Si-substrate (blue) and the 3.6 µm thick a-Si layer (yellow) different material parameters and initial stresses were implemented.

Different material properties were used for the c-Si substrate (blue colored in Figure 3) and a-Si layer (yellow colored in Figure 3), respectively. A potential thermal resistivity at the a-Si/c-Si interface was neglected.

The applied EB line pattern was considered as a moving heat source with a spatial distribution according to the absorbed EB power-depth-relation in Figure 2 (red curve).

To minimize the computational efforts mirror symmetry was exploited and only a selected sample domain was taken into account, at which maximum temperature rise was ≥ 10 K.

As shown in Figure 4 the maximum lateral mesh size was optimized concerning tolerable computation time vs. convergence and was fixed to 300 µm, finally.

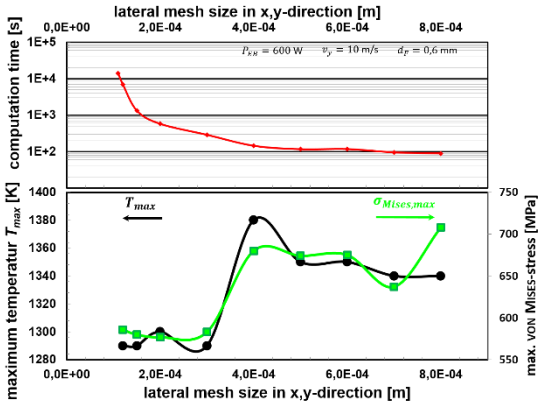

Figure 4: Parametric study for optimization of the mesh geometry. For decreasing lateral mesh size the computation time (red curve) rises nonlinearly, whereas for a lateral mesh size ≤ 300 µm the variations of the maximum values of the temperature T_{max} (black curve) and VON MISES stress (green curve), respectively, are marginal.

5. Theory

Due to different material properties, it is hard to calculate the temperature field of the a-Si/c-Si layer system during EB processing by a numerical model. An adequate expedient constitutes of preliminary melting tests by scribing EB lines on naked Si substrates [14, 15]. Within these tests the conditions will be delimited, at which an initial melting up of the c-Si surface begins ($T_{melt} = 1685$ K). This method takes the advantage of melting phenomena can be detect precisely after EB processing experiment on the one hand. This is because a surface contour is built up due to differences in density and surface tension between liquid and solid Si.

On the other hand, these conditions can be calculated numerically if a quasi-adiabatic state will be reached and thermal conduction can be neglected. The critical energy density e_{crit} for melting up consists of two terms q_s and h_{fus} for heating up form initial temperature and for melting up, respectively (Eq. 8).

$$e_{crit} = q_s + h_{\mathrm{fus}} = 6{,}5 \cdot 10^9\ \mathrm{J/m^3} \qquad \text{Eq. 8}$$

If the maximum of absorbed EB energy density $e_A(x,y)$ (Eq. 9) is equal to e_{crit}, melting will be occur and Eq. 10 should be valid.

$$e_A(x,y) = \frac{1}{R_e} \iint p_A\big(x, y(t),\, z\big)\, \mathrm{d}t\, \mathrm{d}z \qquad \text{Eq. 9}$$

$$P_{EB} = e_{crit} \cdot \frac{R_e \cdot \sqrt{\pi} \cdot r_F}{\eta_{th}} \cdot v_y \qquad \text{Eq. 10}$$

Eq. 10 shows a linear relation and is illustrated by dashed line in Figure 5. The quasi-adiabatic state will be achieved if EB power $P_{EB} = U_B I_B$ and the line scanning speed v_y is high enough to heat up the material to silicon's melting point instantaneously. As also shown in Figure 5, for FEM calculated values (symbols with the solid interpolation lines) there is a small shift to higher P_{EB} because power loses by thermal radiation where also taken into account. For lower P_{EB} and smaller v_y the linear relation is not valid because thermal conduction becomes dominant.

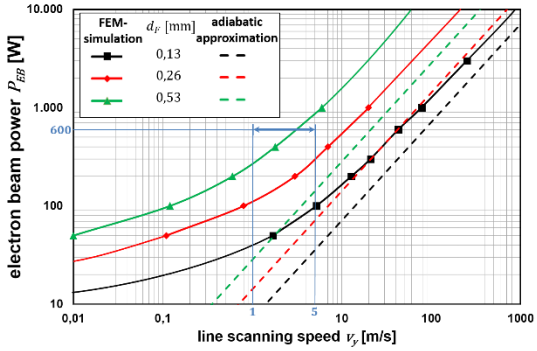

Figure 5: Calculated relation between electron beam power and line scanning speed for the appearance of the first melting phenomena on naked Si wafer for three different beam radii r_F. The symbols with the solid interpolation lines represent the results of FEM simulation, whereas the dashed lines show the linear relationship in a quasi-adiabatic approximation. In blue, the parameter field is highlighted, at which melting phenomena have been observed experimentally.

6. Results

6.1 Experimental Results

Figure 6-a shows an overview optical micrograph of an a-Si coated substrate (a-Si thickness: 3.6 µm), which was EB processed by scanning seven parallel lines with different scanning speed $v_y = 10 \ldots 58\,\mathrm{m/s}$. As shown in the magnified micrograph Figure 6-b, line scanning with small v_y, which corresponds to large energy density $e_A = \int p_A \mathrm{d}t$, leads to delamination of the layer and the formation of detached flakes with a spoke-like microstructure. At $v_y = 26\,\mathrm{m/s}$ delamination occurs only at

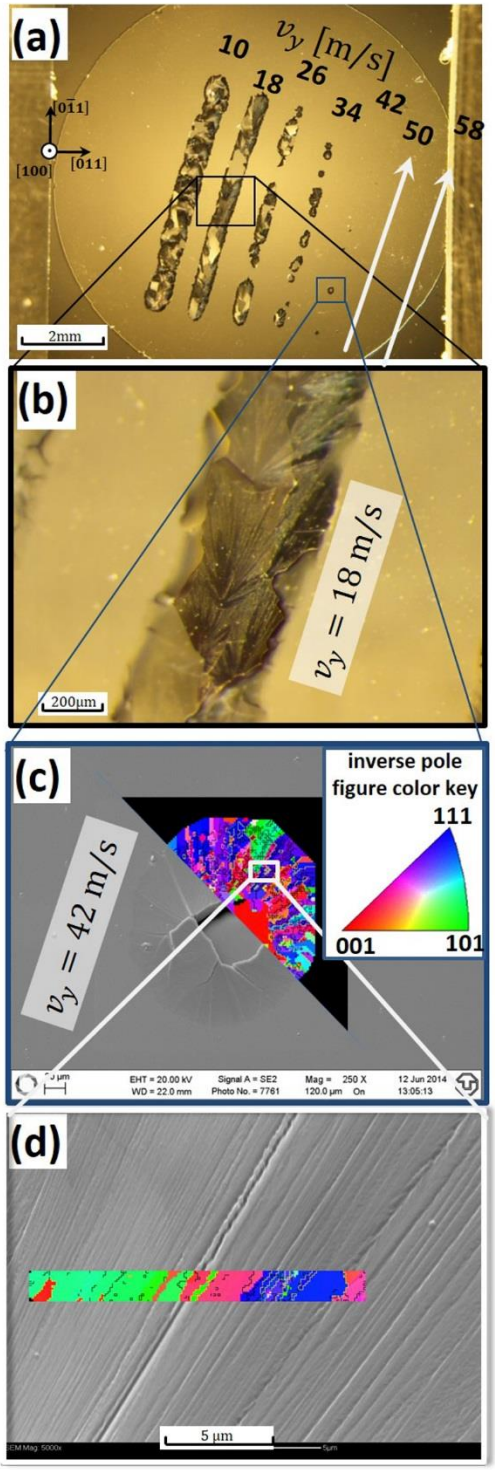

Figure 6: Optical (a, b) and SEM (c, d) micrographs of 3.6 µm thick a-Si layer processed by EB line scans. The overlaid EBSD mappings represent crystal orientation (colored) and amorphousness (black), respectively.

certain areas and disappears completely for $v_y \geq 50\,\mathrm{m/s}$ and $e_A \leq 7\,\mathrm{kJ/cm^3}$, respectively. The scanning electron microscope (SEM) micrograph in Figure 6-c with overlaid electron backscatter diffraction (EBSD) mappings illustrates, that delamination and crystallization is correlated. Layer regions, which are still attached to the substrate, are still amorphous as the black color indicates. In the crystallized region, a fine grained structure with elongated crystallites is build up, showing random orientation (Figure 6-d). This structure without agglomeration is typically for explosive solid phase crystallization.

In contrast to line scanning experiments with high local power input (Figure 6-a...d), additional crystallization tests with extended scanning pattern were carried out on a 1 µm thick a-Si. The EB was scanned frequently for 180 s in the shape of a spiral line pattern with a line pitch $\ll d_F$. The beam power was raised sequentially to maximum, which was 10x lower than for line scanning experiments. This scanning procedure led to slow heating up of almost the whole sample up to $T_{max} = 1500\,\mathrm{K}$, which was measured by pyrometer. Figure 7 shows an overview SEM micrograph of the sample after EB processing at extended scanning area.

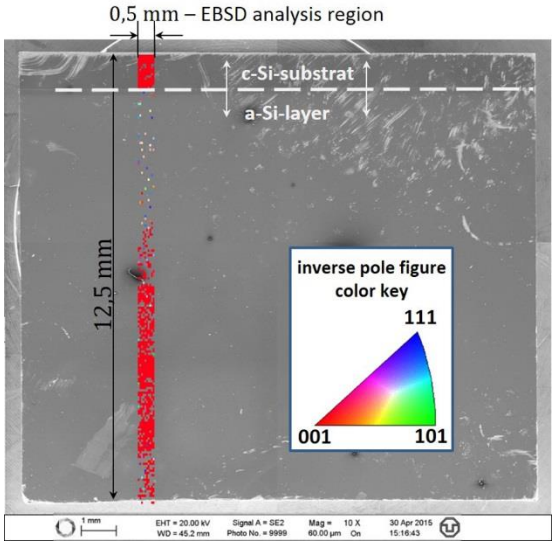

Figure 7: SEM micrograph of 1 µm thick a-Si layer processed by EB scanning pattern over an extended area. The overlaid EBSD mapping in the narrow analysis region represents indicated crystal orientation (colored).

Because of deposition shadowing, the sample's upper part has an uncoated region with naked (001) wafer substrate, which is also illustrated in Figure 7 by the red color of the overlaid EBSD mapping. Due to the decentering of the spiral pattern, the maximum temperature was reached in the lower part of the sample. In mentioned region, the processed layer is still attached to the substrate and epitaxial regrowth to (001) crystal orientation occurred, which is illustrated in Figure 7 by the red color of the overlaid EBSD mapping.

6.2 Numerical Results

To understand the mechanism leading to layer delamination during EB line processing, the knowledge of temperature and thermal induced stress field are significant. Figure 8 shows the FEM-calculated temperature-depth profile in the a-Si/c-Si thin film system for various line scanning speeds v_y at the moment of EB spot passing the sample's midpoint ($y = 0$ m).

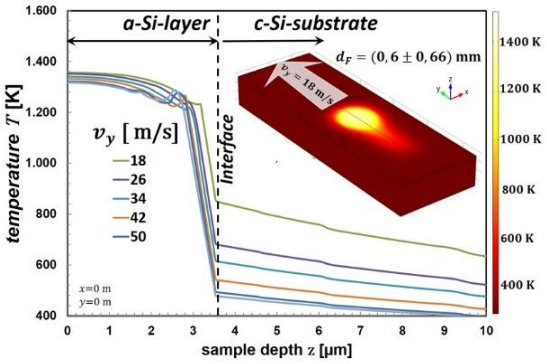

Figure 8: FEM-calculated temperature-depth profile in a-Si/c-Si layer system during EB spot passing for various line scanning speeds. Inset: computed temperature field at $v_y = 18\,\mathrm{m/s}$.

For mentioned moment the inset in Figure 8 illustrates the three-dimensionally calculated temperature field for $v_y = 18\,\mathrm{m/s}$ by color key. Accordingly, the maximum temperature is below the melting point of a-Si ($T_{a-l} = 1420\,\mathrm{K}$ [16]). Therefore, the initiation of explosive solid phase crystallization would not be expected in contrast to experimental results. The inset in Figure 9 illustrates the computed σ_{yy}-component stress field in color key of sample's half-section. Furthermore sample deformation is displayed

100x expanded. The corresponding σ_{yy}- stress component vs. sample depth in Figure 9 shows only a little variation for the maximum stress value in the a-Si layer for investigated v_y.

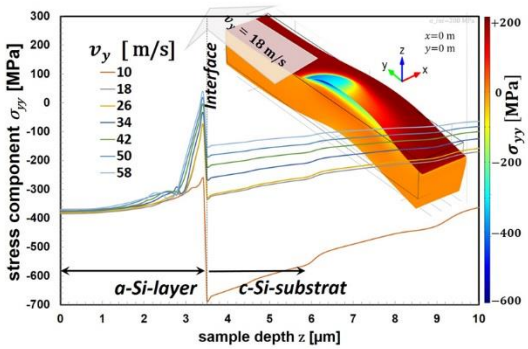

Figure 9: Correlated σ_{yy}-stress component vs. sample depth for various line scanning speeds. Inset: σ_{yy}-stress field with resulting deformation in exaggerated schema.

7. Discussion

Layer delamination will be expected if the stored mechanical energy exceeds the interface energy. Figure 10 shows the elastic strain energy density w_σ vs. applied scanning speed. For $v_y < 50$ m/s, calculated values of $w_\sigma > 0.68\,\mathrm{J/m^2}$ exceed the a-Si/c-Si interface energy [17, 18].

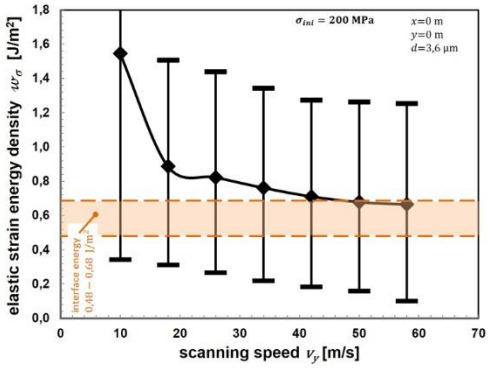

Figure 10: Calculated elastic strain energy density w_σ vs. applied scanning speed. The value range of the a-Si/c-Si interface energy [17, 18] are highlighted for reference.

That means during the experimental EB line processing the a-Si layers spall off due to high elastic energy. Furthermore, delamination will be encouraged by potential oxide film of the non-ideal clean interface. Layer crystallization took place after spalling off because of lower thermal coupling to the c-Si substrate and stronger layer heating. With EB processing by extended scanning pattern at lower EB power, in the EB interaction region the layer grows originated at the substrate interface to a nearly single crystalline structure without layer delamination. Due to the thinner layer thickness, crystallization process may be influenced positively, because:

(i) Corresponding to Figure 2 the maximum of EB power absorption coincide with the substrate interface in this case

(ii) Corresponding to the integral limits in Eq. 3 the accumulation of the strain energy density is more reduced

Epitaxial regrowth occurred in the solid phase regime assuredly, because agglomeration effects were not observed and the measured maximum temperature was 180 K below the melting point of c-Si.

8. Conclusions and Outlook

Comsol® was used for deeper understanding the impact of the electron beam (EB) treatment of coated substrates. For this a model was build up, which agrees very well with theory and experiment. Additional simulation results were compared with investigations by SEM and EBSD analysis. Epitaxial regrowth of 1 µm EB-PVD deposited a-Si layers in the solid phase regime was reached by EB processing with extended scanning pattern. Enhancing throughput's ability by increasing the a-Si thickness and EB power density leads to undesired layer delamination. In further FEM simulations the reason for layer delamination could be revealed by calculating the temperature and stress field during the EB treatment of the thin film–substrate–system: Due to thermal expansion during the EB line scans the elastic strain energy density accumulates and reaches a critical level. If the value exceeds the Si/a-Si interface energy or even the Si surface energy, respectively, layer delamination during the EB process is caused.

To determine process limits, e.g. maximum layer thickness and minimum EB exposure time, further experiments with raised substrate temperatures by preheating, various a-Si film thickness and adapted electron penetration ranges and EB power have to be carried out systematically. Fraunhofer FEP is looking for project partners to clarify unfathomable material aspects and to intensify the research topic.

9. Acknowledgements

The author gratefully acknowledges Prof. Dr. Chr. Metzner, Prof. Dr. J. Weber, Dr. J.-P. Heinß and Dr. D. Temmler for supervising and supporting as well as Prof. Dr. E. Hieckmann for supporting EBSD-analysis.
The project was funded by the European Union and the Free State of Saxony (funding reference 100102018).

10 References

[1] J.-P. Heinß *et al.*, *Proceedings of EU PVSEC 2015*, Hamburg, 3BO.5.4, 1022-1025, (2015)

[2] S. Saager, PhD thesis, TU Dresden, (2015)

[3] C. Becker *et al.*,*Solar Energy Materials and Solar Cells* , vol. **119**, pp. 112-123, (2013)

[4] I. Höger *et al.*, *Proceedings of EU PVSEC 2014*, Amsterdam, 3CO.6.2, 1498-1501, (2014)

[5] D. Amkreutz *et al.*, *Solar Energy Materials and Solar Cells* , vol. **123**, no. 0, pp. 13-16, (2014)

[6] T. Kieliba, PhD thesis, Konstanz, (2006)

[7] J. Haschke *et al.*, *Presentation at EU PVSEC 2014*, Amsterdam, 3CO.6.1, (2014)

[8] T. Pliewischkies *et al.*, *physica status solidi (a)*, vol. **212**, no. 2, pp. 317-322, (2015)

[9] Chr. Metzner *et al.*,, *Novel Method for the Production of Thin Silicon Wafers*, Fraunhofer FEP Annual Report 2014/15, pp.16-19, (2015)

[10] E. Bodenstein & D. Temmler, *Proceedings. of EUPVSEC*, Hamburg, 3DV.2.8, 1287-1289, (2015)

[11] D. Temmler *et al.*, Patent WO2014/117890A1, (2014)

[12] S. Saager *et al.*, *Proceedings of EU PVSEC 2015*, Hamburg, 3BO.6.3, 1036-1041 ,(2015)

[13] J. Kim *et al.*, *Thin Solid Films*, vol. **518**, no. 17, pp. 4908-4910, (2010)

[14] E. Bodenstein, Master thesis, TU Dresden, (2014)

[15] K. Bedrich, Master thesis, TU Freiberg, (2013)

[16] E. P. Donovan *et al.*, *Applied Physics Letters*, vol. **42**, no. 8, pp. 698-700, (1983)

[17] K. Tu, *Applied Physics A*, vol. 53, no. 1, pp. 32-34, (1991)

[18] Z. Jian *et al.*, *Acta Materialia*, vol. 54, no. 12, pp. 3227-3232, (2006)

11. Appendix

Table 1: List of used mathematical symbols

I_B … electron beam current
j_B … electron beam current density
v_y … scanning speed of EB in y-direction
U_B… electron beam acceleration voltage
r_F … electron beam radius $(1/2 \cdot d_F)$
η_{th}… portion of the EB power transferred into heat (ca. 75%)
$f_A(z)$... absorbed power-depth relation (proportional to red curve in Figure 2)
R_e ... electron penetration range
E_{e^-} ... electron beam energy
d_F ... electron beam diameter
c_p ... specific heat capacity
ρ ... mass density
$T, T_{\mathrm{ref}}, T_{melt}, T_{max}$ ... temperature
T_{a-l} ... melting temperature of a-Si
t ... time
$\vec{r}$ ... position vector
λ ... thermal conductivity
P_{EB} ... electron beam power $(= U_B I_B)$
p_A ... absorbed electron power density
h_{fus} ... specific enthalpy of fusion
$\hat{\sigma}$ ... stress tensor
σ_{yy} ... $yy-$ component of the stress tensor
$\hat{\sigma}_{ini} = \begin{pmatrix} \sigma_{ini} & 0 & 0 \\ 0 & \sigma_{ini} & 0 \\ 0 & 0 & 0 \end{pmatrix}$ … initial stress tensor for a-Si layer
$\hat{C}$ ... elasticity tensor
$\hat{\epsilon}^{\sigma}$ ... strain tensor
$\hat{\epsilon}^{\mathrm{th}}$ ... therma strain tensor
w_{σ} ... elastic strain energy density
d ... layer thickness
e_{crit} ... critical energy density for melting up
q_s ... heat density for heating up
$e_A(x, y)$ ... absorbed electron beam energy density